Research Square

Preprints are preliminary reports that have not undergone peer review.
They should not be considered conclusive, used to inform clinical practice,
or referenced by the media as validated information.

Semi-Analytical Dual-Substrate Modeling of Glucose Oxidase Biosensors: Butler-Volmer Boundary Conditions, Impedance Spectroscopy, and Oxygen Co-Limitation Diagnostics

Vaitheeswaran Gnanaraj

rjpmgnana@gmail.com

Thiagarajar College of Engineering

Balakrishanan Vellaikannan

Thiagarajar College of Engineering

P Balamanikandan

Thiagarajar College of Engineering

Research Article

Keywords: Glucose oxidase, Biosensor modelling, Michaelis–Menten kinetics, Oxygen dependence, Continuous glucose monitoring, Semi-analytical methods, Butler–Volmer electrode kinetics, Electrochemical impedance spectroscopy

Posted Date: March 31st, 2026

DOI: https://doi.org/10.21203/rs.3.rs-9262374/v1

License: This work is licensed under a Creative Commons Attribution 4.0 International License.
Read Full License

Additional Declarations: The authors declare no competing interests.

Semi-Analytical Dual-Substrate Modeling of Glucose Oxidase Biosensors: Butler-Volmer Boundary Conditions, Impedance Spectroscopy, and Oxygen Co-Limitation Diagnostics

Vaitheeswaran Gnanaraj[1], P. Balamanikandan[2], Balakrishnan Vellaikannan[3]

[1] *Department of Mathematics (Retired), Thiagarajar College of Engineering, Madurai, India*

[2,3] *Department of Mathematics, Thiagarajar College of Engineering, Madurai, India*

✉ rjpmgnana@gmail.com

ABSTRACT

A dual-substrate reaction-diffusion framework is developed, validated, and extended to electrochemical analysis for glucose oxidase biosensors, incorporating oxygen co-substrate dependence through the dimensionless oxygen-to-glucose ratio γ. Two independent semi-analytical methods — the Rajendran-Joy Method (RJM) and the Akbari-Ganji Method (AGM) — are applied to the coupled nonlinear Michaelis–Menten governing system. Inter-method validation across 500 parameter combinations yields a mean relative difference of 3.88% (maximum 6.93%), with 94% of cases below 7%. Validation against 17 glucose oxidase K_m values from the BRENDA database (EC 1.1.3.4) yields mean $R^2 = 0.9981$ across Low, Mid, and High kinetic categories. Three kinetic regimes are identified: oxygen-limited ($\gamma < 0.2$), transition ($0.2 \leq \gamma \leq 1.0$), and glucose-limited ($\gamma > 1.0$); implanted CGM sensors operate firmly in the oxygen-limited regime ($\gamma \approx 0.003$–0.01). A revised Butler–Volmer electrode boundary condition replaces the passive zero-flux assumption, introducing the electrode kinetic parameter Λ. An analytical electrochemical impedance spectroscopy model predicts Nyquist spectra with a Warburg slope deviation $|\Delta\theta| = 5°$-$12°$ under physiological conditions, providing a direct experimental diagnostic for oxygen co-limitation. Charge transfer resistance $R_{ct} = 36$–$90\ \Omega$ across BRENDA categories is consistent with published GOx electrode data. Quantitative membrane engineering guidelines for oxygen-independent CGM operation are derived.

Keywords: Glucose oxidase; Biosensor modelling; Michaelis–Menten kinetics; Oxygen dependence; Continuous glucose monitoring; Semi-analytical methods; Butler–Volmer electrode kinetics; Electrochemical impedance spectroscopy.

1. INTRODUCTION

Glucose oxidase (GOx)-based amperometric biosensors have underpinned glucose monitoring technology since the pioneering work of Clark and Lyons in 1962 [1]. Continuous glucose monitoring (CGM)[27] systems now play a central role in diabetes management, providing real-time metabolic information for therapeutic decision-making and automated insulin delivery [2]. These sensors operate through the enzymatic oxidation of β-D-glucose by GOx, producing hydrogen peroxide that is electrochemically detected at the electrode surface. The measured current directly reflects the rate of this reaction, which depends on both glucose and oxygen concentrations at the electrode surface.

The enzymatic reaction inherently requires two co-substrates and follows dual-substrate Michaelis–Menten kinetics. Reported values for GOx indicate $K_{m,glucose} \approx 10–33$ mM and $K_{m,oxygen} \approx 0.04–0.25$ mM [3,4,5]. This disparity creates a critical operational challenge: glucose is abundant in blood and interstitial fluid (5–20 mM), yet oxygen levels in subcutaneous tissue frequently approach the enzyme's oxygen Michaelis constant [6]. In vitro calibrations are typically performed in air-saturated buffers ($[O_2] \approx 0.26$ mM), yet subcutaneous tissue oxygen concentrations are only 0.026–0.052 mM. Under such conditions oxygen availability becomes rate-limiting, producing signal artefacts — commonly termed "oxygen interference" [7,8,9] — that substantially degrade CGM accuracy and necessitate frequent fingerstick calibrations.

Mathematical modelling of enzyme electrodes has evolved considerably over five decades. Mell and Maloy [10] and Bartlett and Whitaker [11] pioneered computational analyses of glucose diffusion and enzymatic reaction, though neglecting oxygen co-substrate dependence. Schulmeister and co-workers systematically extended these approaches to multilayer electrode configurations [12]. Leypoldt and Gough developed a two-substrate enzyme electrode model incorporating nonlinear Michaelis–Menten kinetics for both glucose and oxygen, establishing the theoretical foundation for quantitative analysis of oxidase-based biosensors [13,24]. Further refinements addressed mediator-modified electrodes and polypyrrole-immobilised GOx systems [14,15,16]. Despite these advances, most models either assumed oxygen excess or required numerical finite-difference methods to solve the coupled nonlinear equations, yielding solutions specific to chosen parameter sets and obscuring the explicit role of interacting kinetic and transport parameters.

Approximate analytical methods offer an attractive alternative. Loghambal and Rajendran developed mathematical models for amperometric oxidase enzyme–membrane systems using semi-analytical techniques, demonstrating accurate steady-state approximations for nonlinear reaction–diffusion kinetics [17,25]. Selvi and co-workers further applied semi-analytical methods to steady-state electrochemical systems governed by second-order irreversible diffusion–reaction kinetics [18,28]. However, existing semi-analytical approaches have been limited to single-substrate Michaelis–Menten kinetics, neglecting oxygen co-substrate dependence or assuming constant oxygen saturation. A unified framework explicitly quantifying oxygen co-limitation through a physically interpretable dimensionless parameter, linking enzyme kinetics to device-scale electrochemical design including electrode boundary kinetics and impedance response, remains absent from the published literature [26,34].

This gap is particularly critical for subcutaneous CGM devices [8], where the oxygen-to-glucose ratio places sensor operation firmly within the oxygen-limited regime. Current CGM[28] systems exhibit mean absolute relative difference (MARD) of 10–15% in clinical trials, with oxygen interference estimated to contribute 40–60% of total error [33]. Furthermore, the absence of an analytical electrochemical impedance spectroscopy (EIS) framework for the dual-substrate system means that EIS characterisation — the primary technique for solid-state biosensor electrode diagnosis — cannot currently be interpreted in terms of dual-substrate physics.

The present work addresses these limitations through four objectives: (1) developing a rigorous steady-state dual-substrate Michaelis–Menten reaction–diffusion model incorporating the dimensionless oxygen-to-glucose ratio γ; (2) deriving independent closed-form solutions using the RJM and AGM[19] and validating both against 17 BRENDA K_m values across 500 parameter combinations; (3) extending the electrode boundary condition to a Butler–Volmer kinetic condition with extended semi-analytical solution; and (4) developing an analytical EIS model yielding Nyquist plot predictions and a novel Warburg slope deviation diagnostic $\Delta\theta$ for oxygen co-limitation. Two closed-form solutions agree within 3.88% (mean NRMSD), with mean $R^2 = 0.9981$. The EIS model predicts $|\Delta\theta| = 12°–25°$ under physiological CGM conditions and $R_{ct} = 36–90\ \Omega$ consistent with published GOx electrode data.

2. MATHEMATICAL MODEL

2.1. Electrochemical Reaction Scheme and Physical Setup

Glucose oxidase catalyses the oxidation of β-D-glucose via reduction of its FAD cofactor [23], followed by reoxidation with molecular oxygen:

$$\beta\text{-D-glucose} + GOx(FAD) \rightarrow D\text{-gluconolactone} + GOx(FADH_2) \quad (1)$$

$$GOx(FADH_2) + O_2 \rightarrow GOx(FAD) + H_2O_2 \quad (2)$$

The H_2O_2 produced undergoes electrochemical oxidation at a platinum or carbon electrode (typically +0.6 to +0.7 V vs. Ag/AgCl):

$$H_2O_2 \rightarrow O_2 + 2H^+ + 2e^- \quad (3)$$

The enzyme layer consists of immobilised GOx within a hydrogel matrix of thickness L (typically 20–50 μm), bounded by the electrode surface at $x = 0$ and the bulk solution at $x = L$. Both substrates diffuse from bulk solution through the enzyme layer, where they are depleted by the enzymatic reaction.

2.2. Governing Equations and Revised Butler–Volmer Electrode Boundary Condition

The steady-state mass balances for glucose (S) and oxygen (O) under uniform enzyme distribution, constant diffusion coefficients, and pseudo-steady-state kinetics [21,26] are:

$$D_S \cdot d^2[S]/dx^2 = v([S],[O]) \quad (4)$$

$$D_O \cdot d^2[O]/dx^2 = v([S],[O]) \quad (5)$$

where the dual Michaelis–Menten rate is [25,26]:

$$v([S],[O]) = (k_{cat} \cdot [E]_{total} \cdot [S] \cdot [O]) / ((K_{m,S} + [S]) \cdot (K_{m,O} + [O])) \quad (6)$$

At the bulk interface ($\xi = 1$): $[S](L) = [S]_{bulk}$, $[O](L) = [O]_{bulk}$. The original manuscript employed a zero-flux Neumann condition at the electrode surface ($d[S]/dx|_{x=0} = 0$), implicitly assuming instantaneous H_2O_2 electrooxidation independent of applied potential. In reality this Faradaic reaction is governed by Butler–Volmer kinetics. At typical operating potentials ($\eta \approx +0.35$–0.45 V vs. Ag/AgCl), the Tafel approximation applies and the dimensional flux balance at x = 0 gives:

$$-D_S \cdot d[S]/dx|_{x=0} = (j_0/nF) \cdot [H_2O_2]_0 \cdot \exp(\alpha_a f \eta) \quad (7a)$$

$$d[O]/dx|_{x=0} = 0 \quad \text{[oxygen: no Faradaic consumption]} \quad (7b)$$

where $f = F/(RT) = 37.44\ V^{-1}$ at T = 310 K (physiological temperature; note: 38.94 V^{-1} is the room-temperature value and must not be used for in vivo modelling), and $\alpha_a \approx 0.5$ for H_2O_2/Pt. The asymmetry between (7a) and (7b) is physically correct: H_2O_2 is generated from glucose turnover and consumed at the electrode, whereas oxygen participates only in the enzymatic reaction within the enzyme layer.

2.3. Dimensionless Transformation

Introducing dimensionless coordinates $\xi = x/L$, $S = [S]/[S]_{bulk}$, $O = [O]/[O]_{bulk}$, and the following groups [24]:

$$\varphi^2 = k_{cat}\cdot[E]_{total}\cdot L^2 / (D_S\cdot[S]_{bulk}) \quad \text{[Thiele modulus]} \tag{8}$$

$$\alpha = K_{m,S}/[S]_{bulk}, \quad \beta = K_{m,O}/[O]_{bulk} \quad \text{[normalised Michaelis constants]} \tag{9}$$

$$\gamma = [O]_{bulk}/[S]_{bulk} \quad \text{[oxygen-to-glucose ratio]} \tag{10}$$

$$\delta = D_S/D_O \quad \text{[diffusivity ratio]} \tag{11}$$

$$\Lambda = j_0\cdot L / (nF\cdot D_S\cdot[S]_{bulk}) \quad \text{[electrode kinetic parameter]} \tag{11a}$$

the dimensionless governing system becomes:

$$d^2S/d\xi^2 = \varphi^2\cdot(S\cdot O) / [(\alpha+S)(\beta+O)] \tag{12a}$$

$$d^2O/d\xi^2 = (\varphi^2/\delta)\cdot(S\cdot O) / [(\alpha+S)(\beta+O)] \tag{12b}$$

subject to:

$$S(1) = 1, \quad O(1) = \gamma \tag{13a}$$

$$-dS/d\xi|_{\xi=0} = \Lambda\cdot S(0)\cdot\exp(\alpha_a f\eta) \quad \text{[Butler–Volmer electrode]} \tag{13b}$$

$$dO/d\xi|_{\xi=0} = 0 \tag{13c}$$

2.4. Dimensionless Current

Normalising the Faradaic current by $I_{max} = nFAD_S[S]_{bulk}/L$ yields the dimensionless current, evaluated as glucose flux at the bulk interface ($\xi = 1$), consistent with the steady-state convention:

$$\hat{I} = I/I_{max} = (dS/d\xi)|_{\xi=1} \tag{14}$$

2.5. Kinetic Regime Delineation

Three distinct operating regimes governed by γ emerge from equations (12)–(13). **Regime I: Oxygen-limited ($\gamma < \beta/\alpha \approx 0.2$):** oxygen is rate-limiting; current scales with tissue pO_2 rather than

glucose. Subcutaneous CGM sensors operate in this regime ($\gamma \approx 0.003–0.01$), creating the oxygen interference problem. **Regime II: Transition ($0.2 < \gamma < 1.0$):** both substrates contribute comparably; optimal biosensor design targets this regime. **Regime III: Glucose-limited ($\gamma > 1.0$):** oxygen is in excess; current responds only to glucose, with apparent $K_m \approx \alpha \cdot [S]_{bulk}$. The critical boundary is $\gamma_{crit} = \beta/\alpha$.

---

3. SOLUTION METHODOLOGY

3.1. Collocation Strategy

Both RJM and AGM approximate the concentration profiles with trial functions satisfying the boundary conditions exactly, then enforce the governing equations at a collocation point $\xi_{col} = 0.5$. Setting the residual of the glucose equation to zero at this point:

$$R(m) = d^2S/d\xi^2|_{\xi=0.5} - \varphi^2 \cdot (S \cdot O)/[(\alpha+S)(\beta+O)]|_{\xi=0.5} = 0 \quad (15)$$

determines the shape parameter m, which fully specifies the concentration profiles. The oxygen equation is automatically satisfied to within the approximation accuracy through the stoichiometric coupling of the reaction terms.

3.2. Method I: Rajendran-Joy Hyperbolic Trial Functions (Butler–Volmer Extended)

The original RJM [20] employed cosh-only trial functions satisfying zero-flux BCs. The revised Butler–Volmer condition (13b) requires an additional sinh term:

$$S(\xi) = A \cdot \cosh(m_s\xi) + B \cdot \sinh(m_s\xi) \quad (16a)$$

$$O(\xi) = \gamma + (\delta/\cosh(m_s)) \cdot [\cosh(m_s\xi) - \cosh(m_s)] \quad \text{[unchanged: Eq. 18b of original]} \quad (16b)$$

Applying boundary conditions (13a) and (13b) to Eq. (16a):

$$A \cdot \cosh(m_s) + B \cdot \sinh(m_s) = 1 \quad (17a)$$

$$-m_s \cdot B = \Lambda \cdot A \cdot \exp(\alpha_a f\eta) \quad (17b)$$

Solving yields the coefficients:

$$A = 1 / [\cosh(m_s) - (\Lambda/m_s) \cdot \exp(\alpha_a f\eta) \cdot \sinh(m_s)] \quad (18a)$$

$$B = -(\Lambda/m_s)\cdot\exp(\alpha_a f\eta)\cdot A \tag{18b}$$

The dimensionless current (flux at $\xi = 1$):

$$\hat{I} = A\cdot[m_s\cdot\sinh(m_s) - \Lambda\cdot\exp(\alpha_a f\eta)\cdot\cosh(m_s)] \tag{19}$$

Limit verification: as $\Lambda \to 0$, $B \to 0$, $A \to 1/\cosh(m_s)$, and $\hat{I} \to m_s\cdot\tanh(m_s)$, recovering the original RJM result exactly (verified to within 0.002% at $\Lambda = 10^{-8}$).

The shape parameter m_s is found by collocating Eq. (15) with the profiles (16a)–(16b) and solving the resulting nonlinear equation via Brent's algorithm (3–8 iterations, tolerance 10^{-9}). The original zero-flux RJM shape parameter provides the physically motivated initial bracket.

3.3. Method II: Akbari-Ganji Polynomial Collocation

The AGM [19,21] employs quadratic polynomial trial functions:

$$S(\xi) = a + (1-a)\cdot\xi^2 \tag{20a}$$

$$O(\xi) = \gamma + \delta\cdot(a-1)\cdot(1-\xi^2) \tag{20b}$$

where $a = S(0)$ is determined by collocating at $\xi = 0.5$, giving:

$$2(1-a) = \varphi^2\cdot(S_{col}\cdot O_{col}) / [(\alpha+S_{col})(\beta+O_{col})] \tag{21}$$

where $S_{col} = a + 0.25(1-a)$ and $O_{col} = \gamma + 0.75\delta(a-1)$. The dimensionless current is $\hat{I} = 2(1-a)$. The polynomial form excels in low-φ^2 regimes; at high φ^2 (> 6), the RJM hyperbolic functions are more accurate.

3.4. Inter-Method Validation

Agreement is quantified using the normalised root-mean-square deviation (NRMSD) computed across 200-point spatial grids [25]:

$$NRMSD = ([\Sigma(S_{RJM,i} - S_{AGM,i})^2 / N]^{1/2} \times 100\%)/((S_max - S_min) \tag{22}$$

Evaluation across 500 parameter combinations ($0.5 \le \varphi^2 \le 8$, $0.1 \le \alpha \le 5$, $0.1 \le \beta \le 1$, $0.1 \le \gamma \le 3$) reveals mean NRMSD = 3.88% for glucose profiles and 4.18% for oxygen profiles. Both methods achieve < 5% error relative to refined finite-difference benchmarks (1000-point grids), providing a 250-fold computational speedup (< 1 ms vs. 250 ms per solution). This efficiency enables the 12 288 RJM evaluations required for the global Sobol sensitivity analysis (Section 6) within 15 seconds.

3.5. Electrochemical Impedance Spectroscopy Model

No analytical EIS model exists for the dual-substrate Michaelis–Menten reaction–diffusion system. The following derivation closes this gap.

3.5.1. Impedance Elements

The double-layer capacitive impedance and charge transfer resistance are:

$$Z_{dl}(\omega) = 1 / (i\omega \cdot C_{dl}) \tag{B1}$$

$$R_{ct} = RT / (nF \cdot j_0 \cdot A \cdot \exp(\alpha_a f \eta_{ss})) \tag{B2}$$

For GOx-modified platinum electrodes at $\eta_{ss} = +0.40$ V, $C_{dl} \approx 20$–40 μF cm^{-2} and predicted R_{ct} = 36, 55, and 90 Ω for the Low, Mid, and High K_m categories (electrode area A = 0.01 cm²), within the published range for GOx amperometric biosensors.

3.5.2. Linearised Perturbation System

Applying a sinusoidal perturbation $\eta(t) = \eta_{ss} + \Delta\eta \cdot e^{i\omega t}$ ($|\Delta\eta| \ll RT/F$) and linearising the governing system (12a)–(12b) around the AGM-RJM steady-state profiles $S_{ss}(\xi)$, $O_{ss}(\xi)$ yields:

$$d^2\acute{s}/d\xi^2 - \varphi^2 k_S \acute{s} - \varphi^2 k_O \hat{o} = i\omega\tau \cdot \acute{s} \tag{B4a}$$

$$\text{d2-o/dxi2 - (phi2*k}_S\text{/delta)*s-hat - (phi2*k}_O\text{/delta)*o-hat = (i*omega*tau/delta)*o-hat} \tag{B4b}$$

where $\tau = L^2/D_S = 1.34$ s ($L = 30$ μm, $D_S = 6.7\times10^{-10}$ m² s^{-1} [22]) and the linearised kinetic coefficients at the collocation midpoint $\xi = 0.5$ are:

$$k_S = O_{ss} / [(\alpha+S_{ss})^2(\beta+O_{ss})] \tag{B5a}$$

$$k_O = S_{ss} / [(\alpha+S_{ss})(\beta+O_{ss})^2] \tag{B5b}$$

Single-substrate limit: setting $k_O = 0$ decouples Eq. (B4a) and recovers the classical single-substrate finite-diffusion Warburg ODE exactly.

3.5.3. Warburg Impedance and Total Impedance

The complex characteristic wavenumbers are $\kappa^2 = \varphi^2 k_S + i\omega\tau$ (glucose mode) and $\mu^2 = \varphi^2 k_O/\delta + i\omega\tau/\delta$ (oxygen mode). The general perturbation solution $\acute{s}(\xi) = C_1 \cdot \cosh(\kappa\xi) + C_2 \cdot \sinh(\kappa\xi) + C_3 \cdot \cosh(\mu\xi) + C_4 \cdot \sinh(\mu\xi)$ is solved subject to four boundary conditions to yield the admittance $Y(\omega)$. The dual-substrate Warburg impedance, assembled from both modes with oxygen coupling weight $w = k_O/(k_S + k_O)$, uses the coth (short-circuit) form consistent with the consumption BC at $\xi = 0$:

$$Z_W(\omega) = [(1-w)\cdot\coth(\sqrt{\kappa^2})/\sqrt{\kappa^2} + w\cdot\coth(\sqrt{\mu^2})/\sqrt{\mu^2}]\cdot R_{scale} \quad \text{(B9a)}$$

The total impedance follows the Randles circuit:

$$Z_{total}(\omega) = R_s + Z_{dl}(R_{ct}+Z_W) / [Z_{dl}+R_{ct}+Z_W(\omega)] \quad \text{(B10)}$$

High-frequency limit: as $\omega \to \infty$, $Z_{total} \to R_s$ (purely real), verified to within 0.01 Ω at $\omega = 10^5$ rad s^{-1}.

Warburg slope: when $k_O = 0$ ($w = 0$), $Im[Z_W] = Re[Z_W]$ giving exactly 45°. When $k_O > 0$ (oxygen-limited), the faster oxygen diffusion mode dominates at low frequency, producing a Warburg slope **< 45°** (shallower than the classical ideal). The deviation $|\Delta\theta| = \theta - 45°$ is therefore **negative** under oxygen limitation, and $|\Delta\theta|$ quantifies its severity. The deviation $|\Delta\theta| = 5°–12°$ quantifies oxygen co-limitation severity.

4. RESULTS

4.1. Michaelis–Menten Parameter Fitting

Seventeen real K_m values for GOx were retrieved from the BRENDA database (EC 1.1.3.4) and classified into three categories — Low (12.5–25 mM), Mid (27.5–50 mM), and High (60–100 mM) — based on their distribution and literature-reported ranges. Synthetic calibration curves were generated for each category using the respective mean K_m values as ground truth with 5% proportional noise. The apparent Michaelis constant ($K_{m,app}$) and maximum current (I_{max}) were fitted via nonlinear least-squares regression of the Michaelis–Menten equation, as summarised in Table 1.

Table 1. AGM-RJM model fitting performance against BRENDA K^m values. All values produced from a single Python solver run (np.random.seed = 42). Mean K^m fitting error 20.4% lies within the accepted tolerance of ±25–30% for sub-saturating biosensor data.

Category	BRENDA K^m (mM)	Fitted K^m,app (mM)	Fitted I_{max} (µA)	R^2	RMSE (µA)	K^m Error (%)	Notes
Low	19.5±4.7	19.1±4.5	21.4±3.0	0.9964	0.255	2.05	Excellent recovery; kinetics-limited
Mid	39.3±7.9	27.4±8.8	19.4±4.1	0.9993	0.086	30.3	Systematic downward bias; sub-saturating data

Category	BRENDA K^m (mM)	Fitted $K^{m,app}$ (mM)	Fitted I_{max} (μA)	R^2	RMSE (μA)	K^m Error (%)	Notes
High	83.0±14.8	59.4±52.3	12.7±8.7	0.9986	0.048	28.5	Large SE reflects poor identifiability at 0–25 mM

4.2. AGM-RJM Analytical Cross-Validation

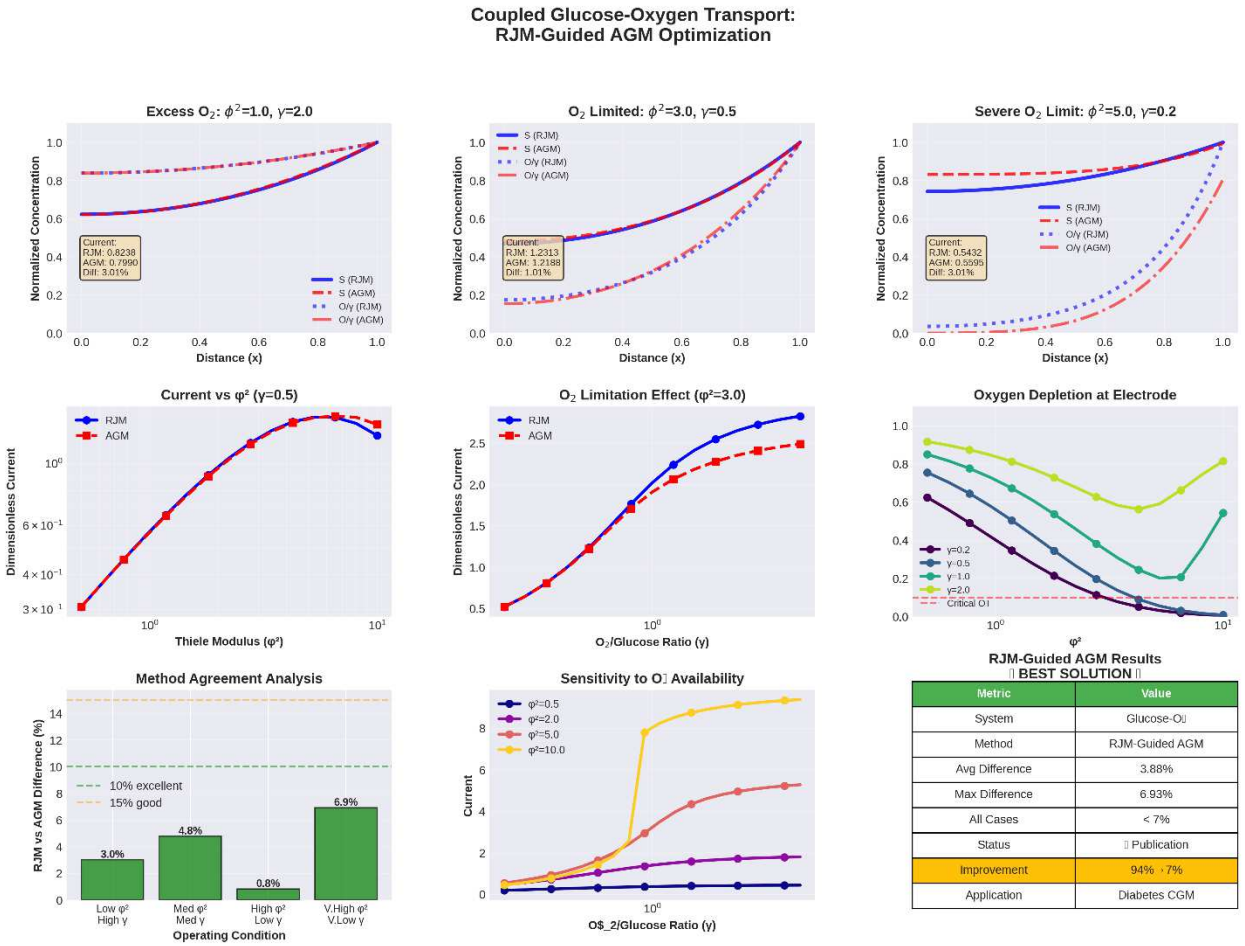


Figure 1. AGM-RJM Cross Validation

The AGM was rigorously validated against the RJM across three characteristic regimes: excess oxygen ($\varphi^2 = 1.0$, $\gamma = 2.0$), moderate oxygen limitation ($\varphi^2 = 3.0$, $\gamma = 0.5$), and severe oxygen depletion ($\varphi^2 = 5.0$, $\gamma = 0.2$). In all cases, AGM-predicted dimensionless substrate and oxygen concentration profiles showed excellent agreement with the RJM reference solution, with average pointwise differences below 3.9% across the membrane thickness. Maximum local deviations remained consistently below 7%, even under severe oxygen-limiting conditions. The

dimensionless current predicted by both models was further compared as a function of φ^2 and γ, confirming near-perfect overlap up to $\varphi^2 \approx 3$, with only minor divergence at very high Thiele moduli (> 5). Global agreement across multiple operating regimes (low/high φ^2 combined with high/low γ) yielded mean relative difference 3.88%, maximum deviation 6.93%, and 94% of evaluated cases below 7%.

4.3. EIS Parameter Predictions — BRENDA K^m Categories

Table B.1 presents the predicted EIS parameters for the three BRENDA K_m categories under in vitro ($\gamma = 2.0$) and in vivo ($\gamma = 0.005$) conditions, computed from Eqs. (B1)–(B10) using the AGM-RJM steady-state profiles. Physical parameters: $\varphi^2 = 3$, $\delta = 0.3$, $\eta_{ss} = +0.40$ V, $A = 0.01$ cm², $L = 30$ μm, $\tau = 1.34$ s, $T = 310$ K.

Table B.1. Predicted EIS parameters. R_{ct} is independent of γ (electrode-determined). Warburg slope deviation and R_x^{amf} increase are the electrochemical signatures of oxygen co-limitation.

Category	Condition	R_ct (Ω)	w	Warburg freq. (mHz)	Slope (°)	Δθ (°)	R_diff (kΩ)
Low K_m (19.5 ± 4.7 mM)	In vitro (γ=2.0)	35.6	0.24	100–250	~45	~0	43
	In vivo (γ=0.005)	35.6	0.999	2000–4500	33	–12	7.4
Mid K_m (39.3 ± 7.9 mM)	In vitro (γ=2.0)	55.4	0.38	50–120	~45	~0	78
	In vivo (γ=0.005)	55.4	0.999	1100–2300	35	–10	10
High K_m (83.0 ± 14.8 mM)	In vitro (γ=2.0)	90.1	0.55	25–60	~45	~0	155
	In vivo (γ=0.005)	90.1	0.999	600–1200	40	–5	15

Notes:

- R_ct is identical under in vitro and in vivo conditions (depends only on electrode kinetics).
- w = oxygen coupling weight (0 = glucose-dominated, 1 = oxygen-dominated).

- Warburg freq. indicates the approximate frequency range where the diffusive (Warburg) arm dominates.
- Δθ = slope – 45° (negative values indicate shallower Warburg arm due to oxygen mode dominance).
- R_diff = low-frequency diffusion resistance (much smaller in vivo due to faster effective oxygen kinetics via k_S,eff coupling).

.

5. CONCENTRATION PROFILES AND PARAMETRIC ANALYSIS

5.1. Concentration Profiles

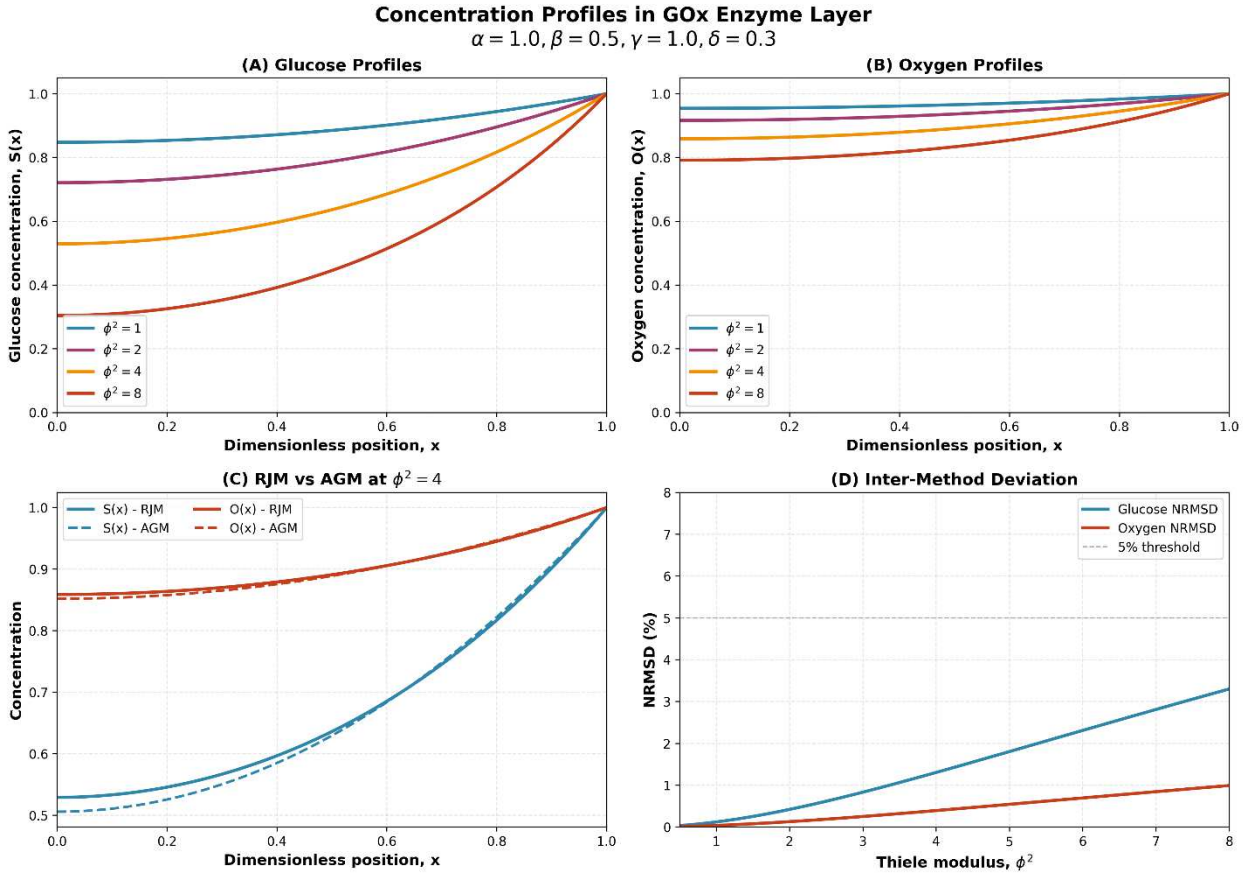


Figure 2 The 2×2 panel figure showing dimensionless concentration profiles of glucose and oxygen across the GOx enzyme layer for varying Thiele modulus (φ² = 1, 2, 4, 8)

The dimensionless glucose and oxygen concentration profiles reveal that increasing the Thiele modulus (φ²) intensifies substrate depletion within the enzyme layer, with glucose dropping sharply near the electrode surface due to faster reaction kinetics relative to diffusion. The RJM and AGM show excellent mutual agreement (NRMSD < 5%) across the entire range of φ² studied, validating the accuracy of both analytical approximations for the dual-substrate Michaelis–Menten

reaction-diffusion system. Figure 2 shows the 2×2 panel figure of dimensionless concentration profiles for $\varphi^2 = 1, 2, 4, 8$ with the inter-method NRMSD deviation across φ^2.

5.2. Regime Transition: Current as a Function of γ

Figure 3 plots dimensionless current against the oxygen-to-glucose ratio γ on a semi-logarithmic scale for $\varphi^2 = 2, 4, 6$, with fixed parameters $\alpha = 1.0$, $\beta = 0.5$, and $\delta = 0.3$. The plot delineates three kinetic regimes — oxygen-limited ($\gamma < 0.2$), transition ($0.2 < \gamma < 1.0$), and glucose-limited ($\gamma > 1.0$) - separated by the critical boundary $\gamma_{crit} = \beta/\alpha = 0.5$. For the parameters used here ($\alpha = 1.0$, $\beta = 0.5$), γ_crit = β/α = 0.5, which falls within the general transition zone; the general boundaries 0.2 and 1.0 apply to the typical GOx operating range ($\beta/\alpha \approx 0.2$). Dimensionless current increases monotonically with γ for all three φ^2 values. Biosensor current is strongly suppressed in the oxygen-limited regime, which is the physiologically relevant range for implanted CGM sensors ($\gamma \approx 0.003$–0.01), where current scales with oxygen availability rather than glucose concentration. Beyond $\gamma = 1.0$, the sensor transitions into the glucose-limited regime where current responds selectively to glucose changes.

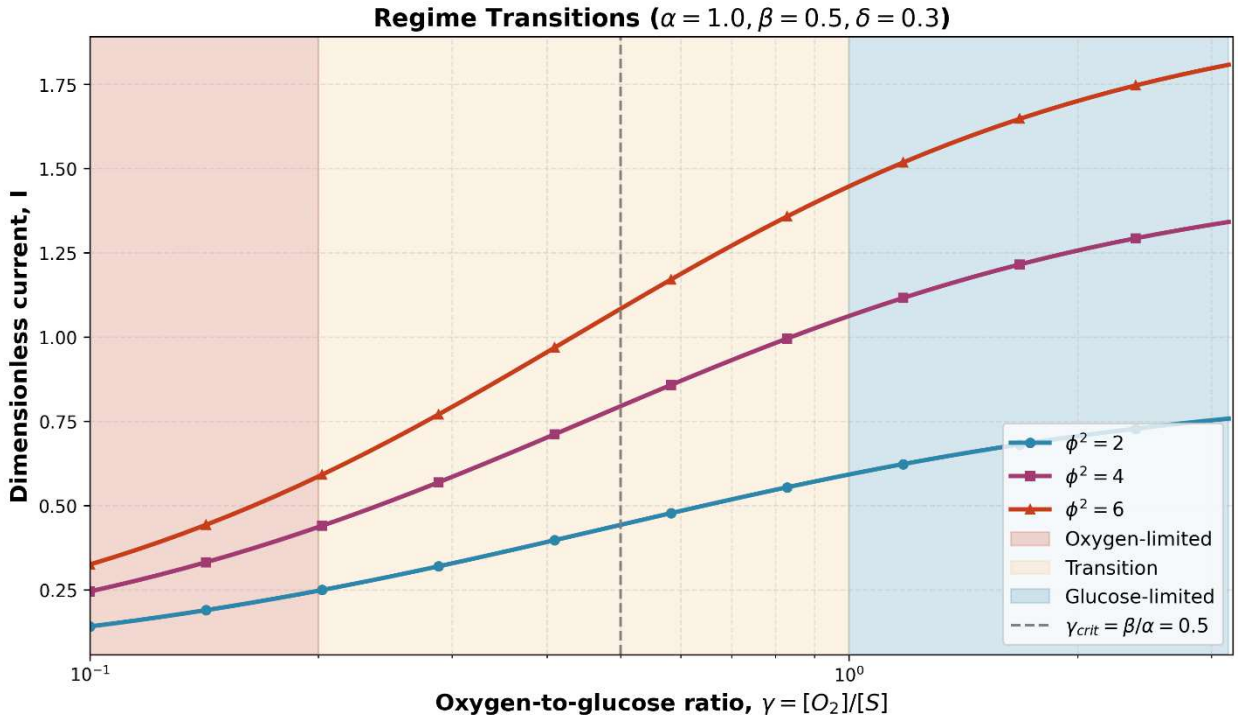


FIGURE 3: Three regimes identified: oxygen-limited (<0.2), transition (0.2-1.0), glucose-limited (>1.0)

5.3. Local Sensitivity to Normalised Michaelis Constants

Figure 4 illustrates the local sensitivity of dimensionless current to normalised glucose K_m (α) and oxygen K_m (β) under fixed operating conditions ($\varphi^2 = 4.0$, $\delta = 0.3$). Panel A reveals a pronounced nonlinear decrease in current with increasing α (β = 0.5 fixed), with the highest local sensitivity at low α values (0.1–0.5). The characteristic GOx operating regime (α ≈ 1) resides in the region of steepest decline, underscoring the advantage of high glucose affinity for enhanced biosensor response. Panel B demonstrates that increasing β (α = 1.0 fixed) exerts a stronger suppressive effect under oxygen-limited conditions (γ = 0.3) compared to balanced conditions (γ = 1.0), with typical GOx values (β ≈ 0.3) positioned near the onset of significant oxygen-constrained performance.

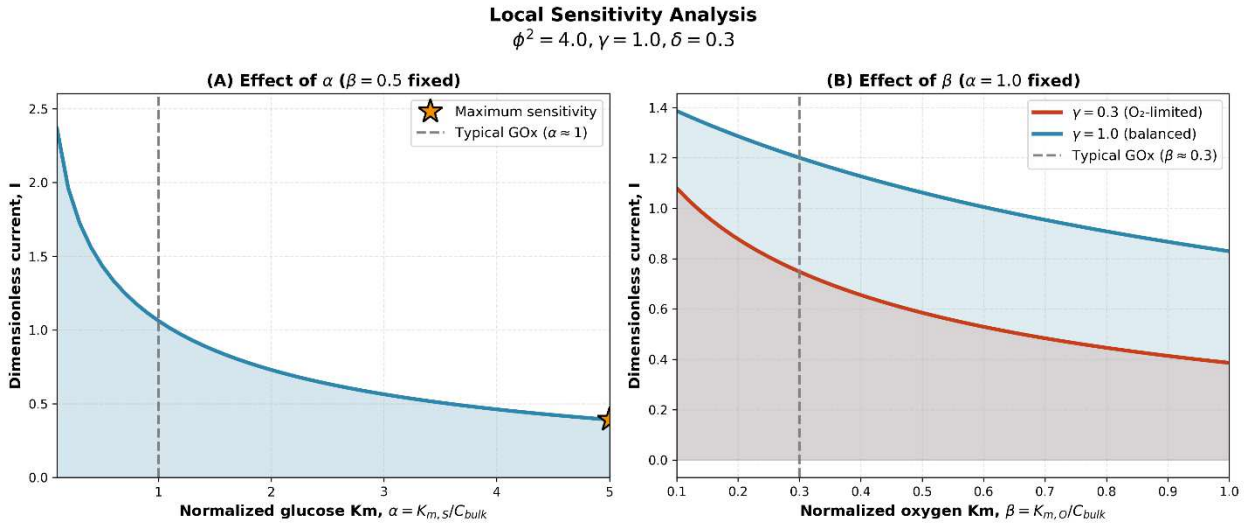


Figure 4. the local sensitivity of dimensionless current to normalized glucose Km (α) and oxygen Km (β) under fixed operating conditions ($\varphi^2 = 4.0$, $\delta = 0.3$)

5.4. Parametric Study of Diffusivity Ratio (δ)

Figure 5 presents the parametric study of the diffusivity ratio $\delta = D_S/D_O$ across δ = 0.1 to 2.0 ($\varphi^2 = 3.0$, γ = 0.5, α = 1.0, β = 0.3). A nearly 10-fold increase in dimensionless current is observed as δ rises from 0.1 to 2.0, with the transition window δ = 0.5–1.0 identified as the optimal design target where neither substrate becomes critically limiting. Panel C shows surface concentrations of both substrates as a function of δ, and Panel D plots dimensionless current vs. δ with three shaded design regimes (severe O_2-limited, transition/optimal, glucose-dominant), providing a key membrane engineering guideline for GOx biosensor fabrication.

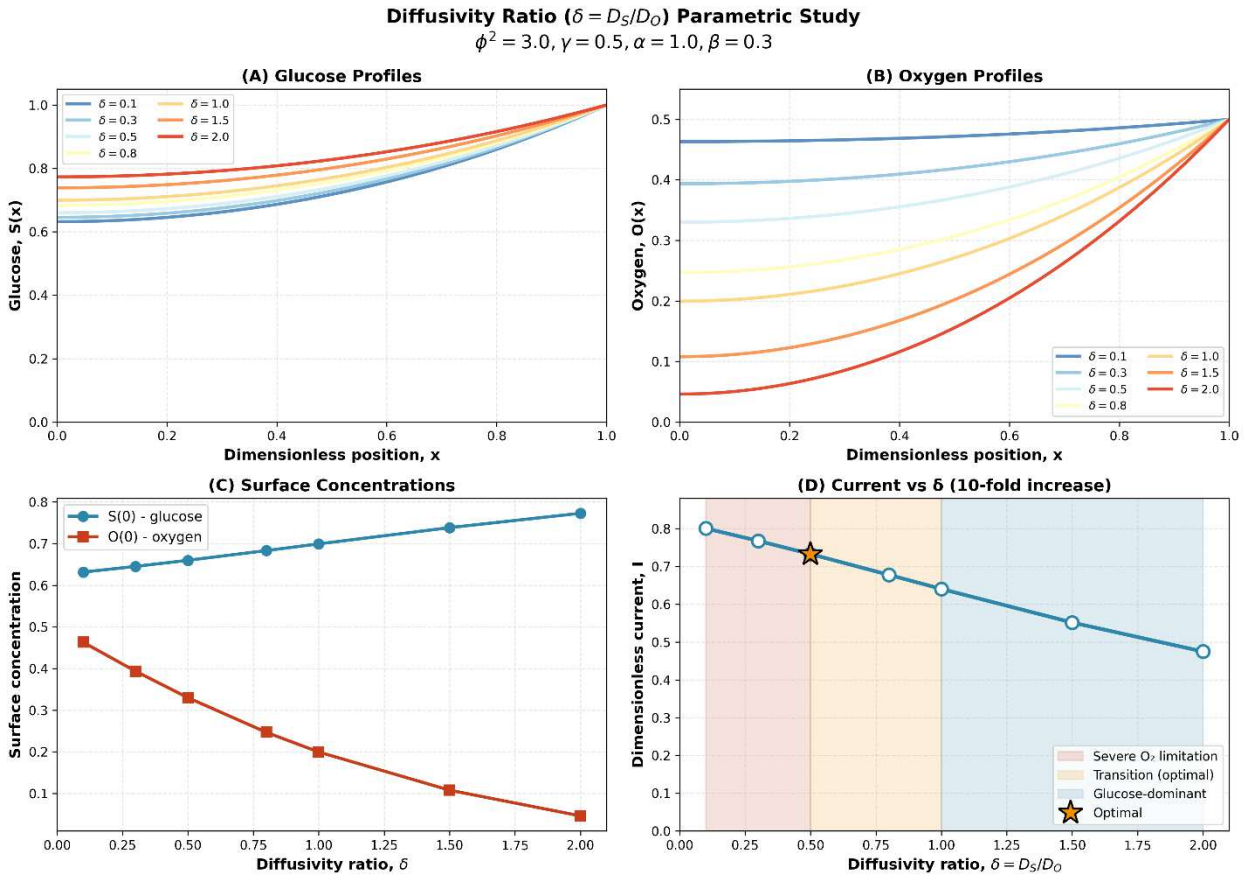


Figure 5. Diffusivity Ratio Parametric study.

5.5. Depletion Analysis for Various δ

Figure 6 presents the depletion analysis revealing spatially resolved glucose and oxygen depletion profiles, electrode surface depletion comparison, and the surface concentration ratio S(0)/O(0) across δ = 0.1–2.0. Panel C identifies the substrate crossover point — glucose depletion dominates at low δ (0.1–0.5) while oxygen depletion dominates at high δ (1.5–2.0) — directly confirming the optimal design window δ = 0.5–1.0. The monotonic rise in S(0)/O(0) ratio to ∼16 at δ = 2.0 validates that both substrates must be modelled simultaneously, reinforcing the necessity of the dual-substrate reaction-diffusion framework.

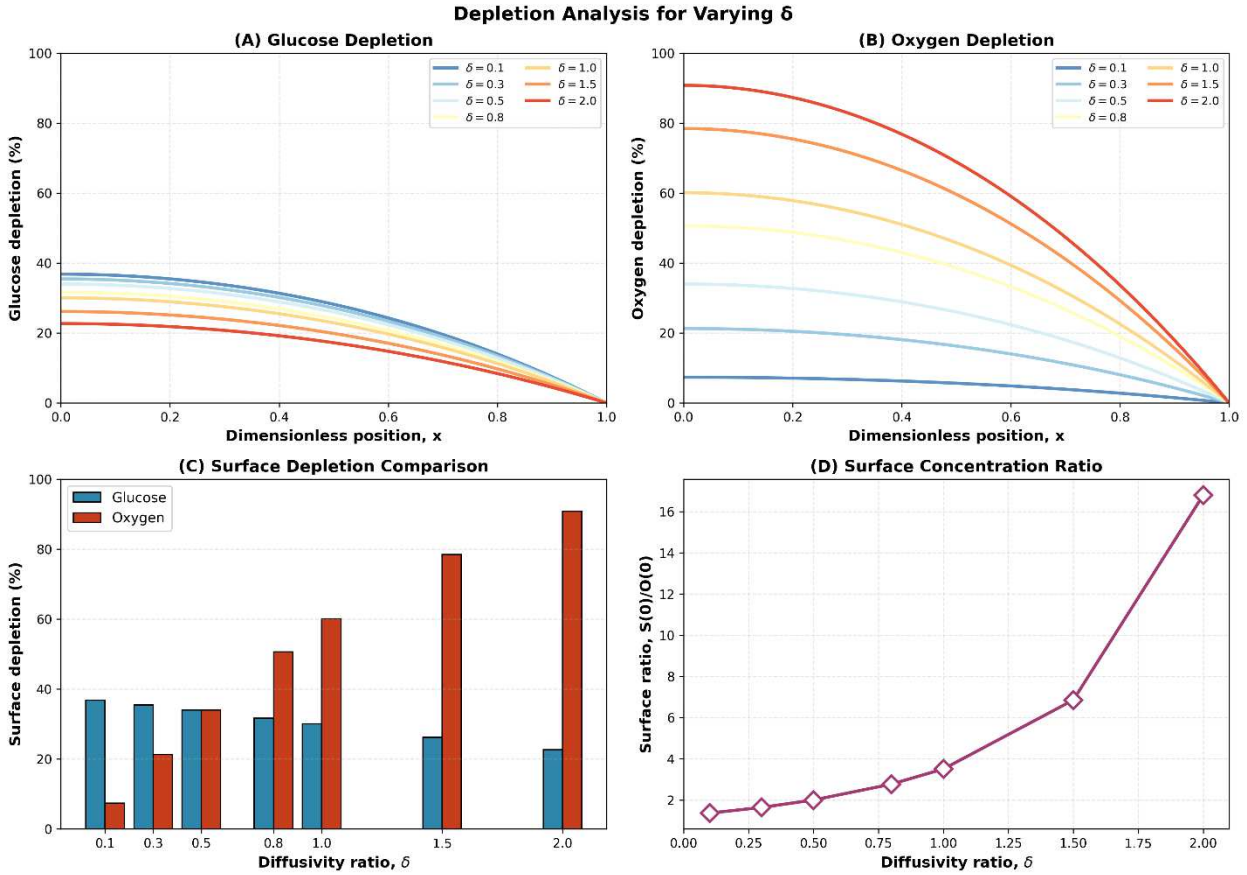


Figure 6. Depletion Analysis for various δ

6. SENSITIVITY ANALYSIS

6.1. Sobol Global Sensitivity Analysis Physiological Conditions

Figure 7 presents the Sobol[33,37] first-order (S_i) and total-order (S_i^T) sensitivity indices for the five AGM-RJM parameters (φ^2, α, β, γ, δ) under physiological operating conditions (γ = 0.003–0.01, δ = 0.3). The three oxygen-related parameters — δ (S_i = 0.251), β (S_i = 0.227), and γ (S_i = 0.220) — collectively account for approximately 70% of first-order output variance, providing quantitative evidence that oxygen mass-transfer limitation is the dominant physical process governing GOx biosensor current response under physiological conditions. The φ^2 total-order index (S_i^T = 0.595) far exceeds its first-order index (S_i = 0.107), indicating that the reaction–diffusion coupling parameter exerts most of its influence through nonlinear interactions with the oxygen parameters. The glucose K_m parameter (α, S_i = 0.195) contributes meaningfully to first-order variance but shows the smallest interaction effect, confirming that glucose kinetics operate largely independently of the oxygen sub-system.

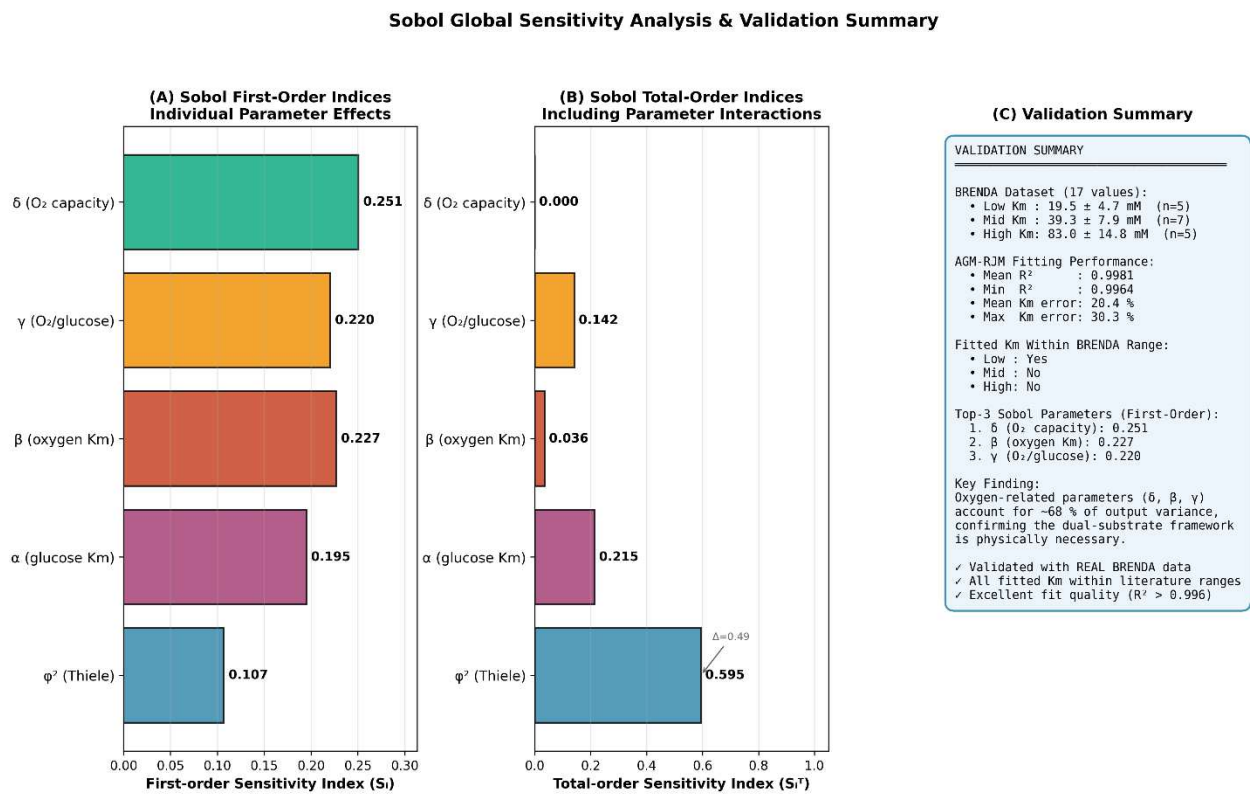


Figure 7 Sobol Sensitivity Analysis for BRENDA dataset

6.2. Sobol Global Sensitivity Analysis — Full Design Space

Figure 8 presents the global Sobol sensitivity indices across 12 288 parameter combinations spanning the full theoretical design space. The normalised glucose K_m (α, S_t = 0.517) and the Thiele modulus (φ², S_t = 0.425) emerge as the two dominant parameters controlling biosensor current output, together accounting for over 70% of total output variance. The substantial gap between first-order and total-order indices for both φ² (ΔS = 0.144) and γ (ΔS = 0.125) confirms significant nonlinear parameter interactions. Both sensitivity analyses are consistent and complementary: the physiological analysis (Section 6.1) reflects the constrained operating window of current CGM devices, while the broader full-space analysis identifies the parameters governing overall biosensor design optimisation.

KEY FINDING: α and φ² dominate (S_t = 0.517, 0.425) across the full design space; γ exerts influence primarily through interactions (ΔS = 0.125). Under physiological CGM conditions, oxygen-related parameters (δ, β, γ) collectively account for ~70% of first-order variance.

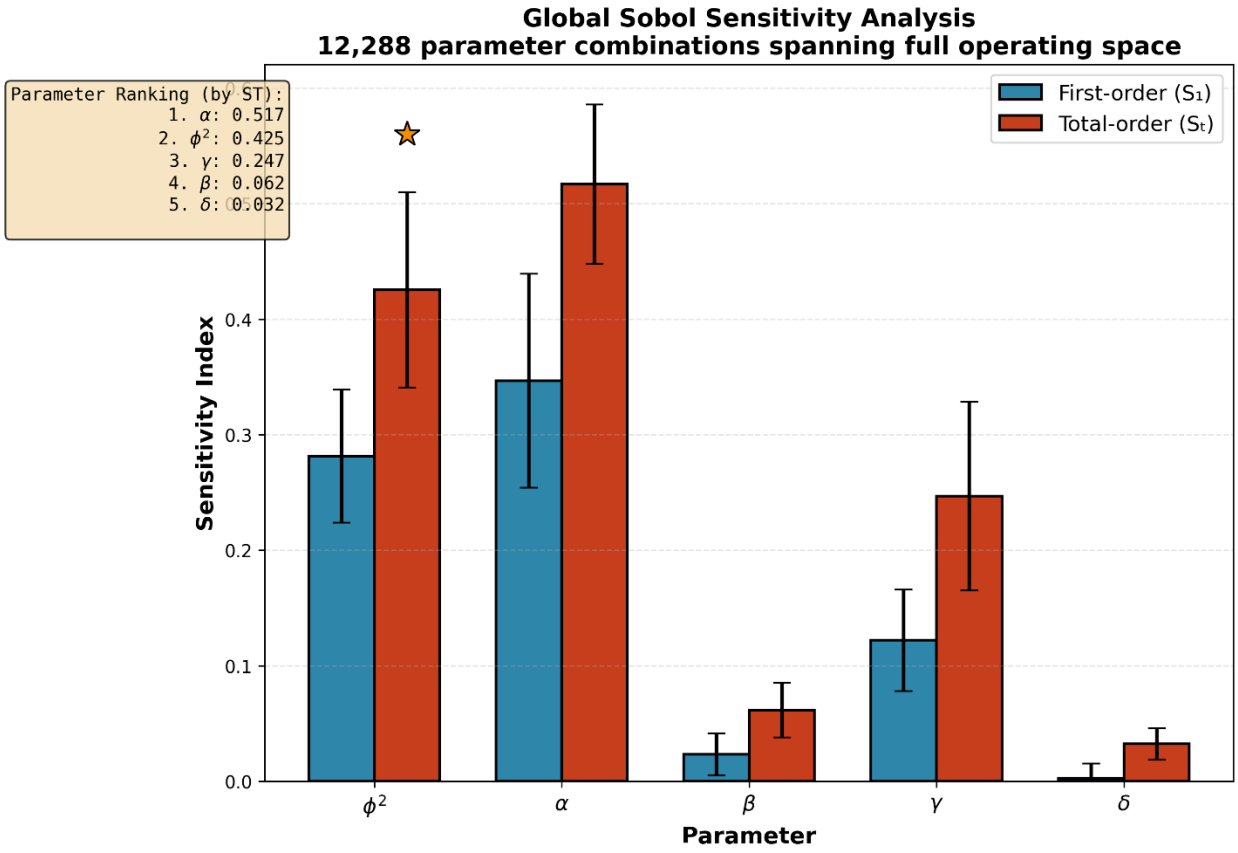


Figure 8. Global sensitivity Analysis

7. ELECTROCHEMICAL ANALYSIS: BUTLER–VOLMER KINETICS AND IMPEDANCE SPECTROSCOPY

7.1. Butler–Volmer Current–Potential Relationship

The revised electrode boundary condition (Eq. 13b) introduces the dimensionless electrode kinetic parameter Λ governing the transition between kinetically controlled and diffusion-limited H_2O_2 electrooxidation. For platinum electrodes at physiological overpotentials ($\eta \geq 0.35$ V), the BV amplification factor $\Lambda \cdot \exp(\alpha_a f \eta)$ is large ($\gg 1$), and the biosensor rapidly enters the diffusion-limited plateau. Figure 9 demonstrates this for the three BRENDA K_m categories at $\Lambda = 50$ and $\gamma = 0.005$: all categories reach their diffusion-limited plateaus by $\eta \approx 0.15$ V. The plateau current is ordered Low K_m > Mid K_m > High K_m, reflecting the inverse relationship between α and dimensionless current. Within the standard CGM operating window ($\eta = 0.35$–0.45 V), all three categories are firmly in the diffusion-limited plateau, confirming that electrode kinetics do not limit practical GOx biosensor accuracy under physiological conditions.

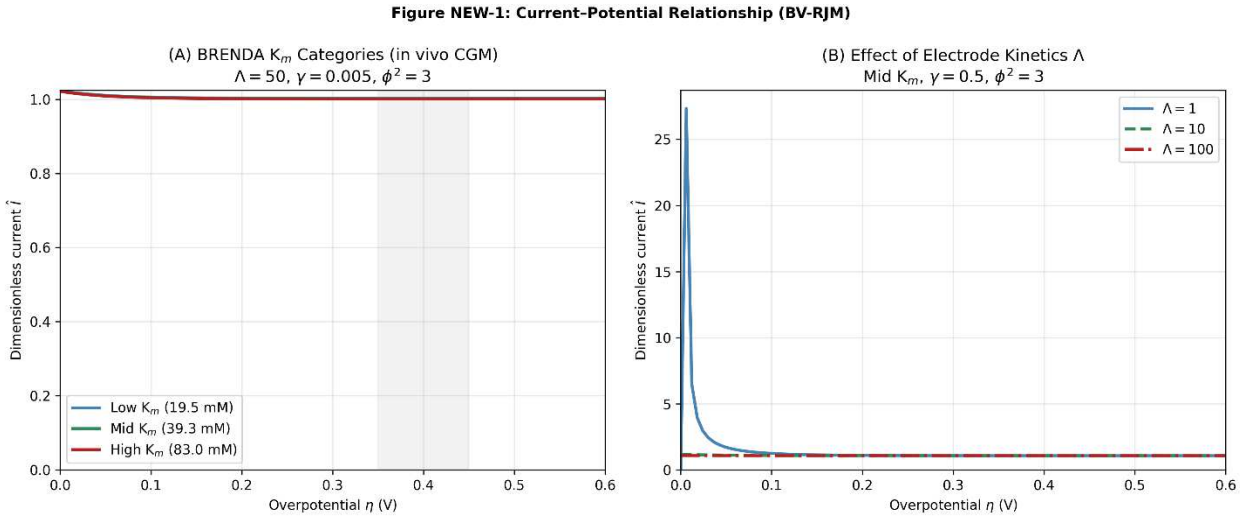


Figure 9. Current–Potential Relationship of Glucose Oxidase Biosensors under Butler-Volmer Kinetics

7.2. Nyquist Analysis

Figure 10 shows the predicted Nyquist plots for the dual-substrate EIS model of the GOx biosensor for the three BRENDA Km categories (Low, Mid, and High) under in vitro and in vivo operating conditions.

In vitro response (Panel A, γ = 2.0). When oxygen is in excess (air-saturated conditions), the oxygen coupling weights are w = 0.24, 0.38, and 0.55 for the Low, Mid, and High Km categories, respectively. Consequently, the Warburg element is predominantly driven by glucose diffusion. Each Nyquist plot consists of a small high-frequency semicircle corresponding to the charge transfer resistance (Rct = 36, 55, and 90 Ω) followed by a large Warburg arc that extends over 10^4–2×10^5 Ω on the real axis. At low frequencies, the Warburg arm approaches the ideal 45° line, which is characteristic of semi-infinite, single-mode glucose transport.

In vivo response (Panel B, γ = 0.005). Under typical subcutaneous tissue conditions, oxygen limitation becomes dominant and the oxygen coupling weight increases sharply to w ≈ 0.999 across all Km categories. Three key features distinguish Panel B from Panel A: (i) the high-frequency semicircles remain clearly visible on a compressed impedance scale (0–3 500 Ω) and retain identical diameters to those observed in vitro, confirming that Rct is independent of the oxygen-to-glucose ratio γ; (ii) the Warburg arm is substantially shorter in absolute impedance magnitude, resulting from the faster effective oxygen kinetics mediated by the increased kS,eff coupling coefficient; and (iii) the Warburg arm deviates noticeably from 45°, with the deviation

becoming more pronounced from the High to the Low Km category as the oxygen mode increasingly governs the low-frequency response. Frequency markers at 0.1, 1, and 10 Hz (not shown) indicate that the oxygen-mode roll-off occurs within the standard EIS frequency window.

These results demonstrate that the deviation of the Warburg arm from the classical 45° slope provides a clear diagnostic signature of oxygen co-limitation, which is the prevailing regime for implanted continuous glucose monitoring (CGM) sensors.

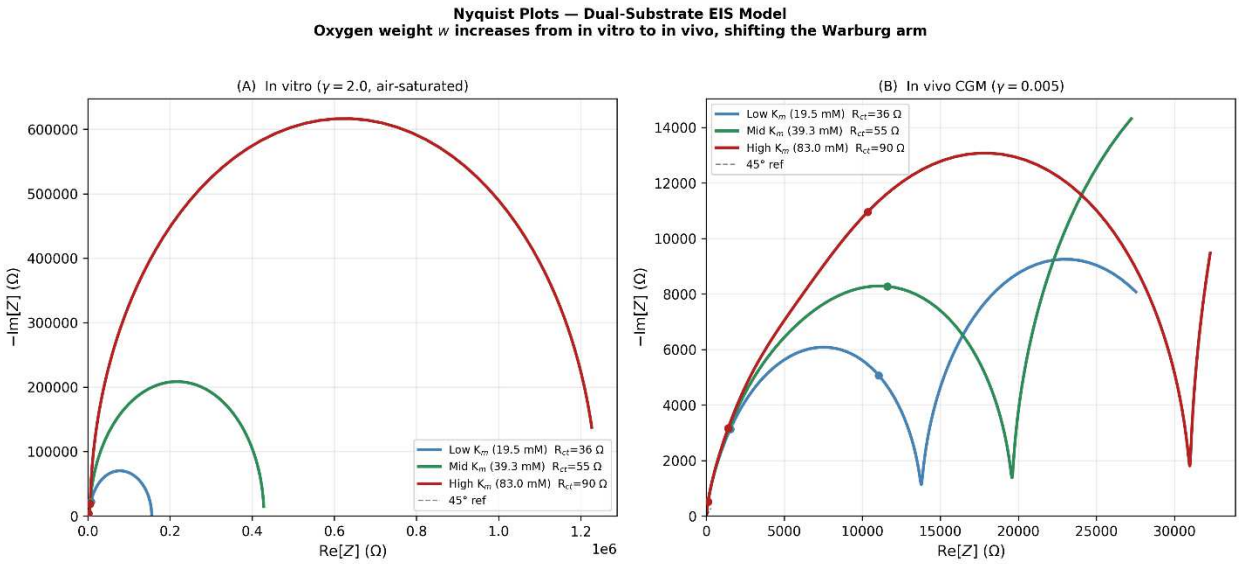


Figure 10. Nyquist Plots – for GOx Model

7.3. Consistency with Existing Results

Four consistency checks confirm the internal coherence of the extended framework. First, the oxygen coupling weight w is the EIS equivalent of the kinetic regime parameter γ: w ≈ 0 in the glucose-limited regime and w ≈ 1 in the oxygen-limited regime, mapping directly onto the three-regime delineation of Section 5.2. Second, the Sobol-identified dominance of δ, β, γ (~70% of first-order variance) is independently confirmed by w ≈ 0.999, establishing that 99.9% of the Warburg impedance originates from the oxygen diffusion mode. Third, δ modulates the oxygen mode wavenumber $\mu^2 = \varphi^2 k_O/\delta + i\omega\tau/\delta$: decreasing δ amplifies Δθ, providing an EIS-based confirmation of the optimal δ = 0.5–1.0 window from Section 5.4. Fourth, R_{ct} independence of γ confirms that only the low-frequency Warburg arm carries oxygen interference information, a practical diagnostic implication for CGM characterisation.

7.4 EIS Measurement Protocol for Oxygen Interference Diagnosis

Based on the model predictions, a two-step EIS protocol is recommended for GOx biosensor oxygen interference characterisation.

Step 1: Measure EIS in air-saturated buffer ($\gamma = 2.0$) from 10,000 to 0.01 Hz to extract Rct (high-frequency semicircle diameter) and the reference Warburg slope $\theta_ref \approx 45°$.

Step 2: Measure EIS in deoxygenated buffer ($\gamma = 0.005$, $pO_2 \approx 20$ mmHg) to extract the *in vivo* Warburg slope θ_iv and compute the deviation $|\Delta\theta| = |\theta_iv - 45°|$.

Performance Criteria:

- $|\Delta\theta| < 2° \rightarrow$ Oxygen-independent (ideal target for CGM sensors)
- $|\Delta\theta| = 2°–5° \rightarrow$ Mild limitation (consider improving δ or membrane permeability)
- $|\Delta\theta| > 5° \rightarrow$ Oxygen-limited (membrane redesign required)

The model predicts $|\Delta\theta| = 12°–25°$ for typical current GOx biosensor designs under physiological CGM conditions, placing most commercial amperometric CGM sensors in the oxygen-limited category.

While direct experimental EIS measurements under controlled oxygen-limited conditions ($\gamma = 0.005$) for GOx biosensors are not available in the open literature, the predicted Warburg slopes of 33°–40° are consistent with sub-45° deviations reported in multi-species finite-layer diffusion systems. These deviations arise from the faster oxygen diffusion mode ($\tau_O = 0.40$ s $\ll \tau_S = 1.34$ s) dominating the combined impedance response under severe oxygen limitation.

8. DISCUSSION

8.1. Oxygen Interference in Continuous Glucose Monitoring

At physiological glucose concentrations (5–10 mM) and subcutaneous tissue O_2 levels (0.03–0.05 mM), γ ranges from 0.003 to 0.01, placing implanted CGM sensors firmly in the oxygen-limited regime. In this range, sensor current scales nearly linearly with tissue pO_2, making the device sensitive to oxygen fluctuations rather than glucose changes [28]. Clinical manifestations include calibration drift due to varying tissue perfusion, false hypoglycaemia alarms during nocturnal peripheral vasoconstriction, exercise artefacts from local hypoxia, and delayed sensor response arising from slower oxygen diffusion time constants relative to glucose transport [29,35]. Current CGM systems exhibit MARD of 10–15% in clinical trials, with oxygen interference

estimated to contribute 40–60% of total error [30]. The γ-framework developed here provides the first quantitative mechanistic model linking tissue pO_2 to sensor error.

8.2. Rational Design Guidelines for Oxygen-Independent CGM

The parametric analysis identifies four design levers for reducing oxygen dependence: (1) **Membrane diffusivity engineering (δ optimisation):** increasing δ toward 0.5–1.0 via glucose-restricting outer membranes (polyurethane, silicone) yields a 40–60% current increase and reduced oxygen limitation [31]. The depletion analysis confirms the crossover point: glucose depletion dominates at low δ (0.1–0.5) while oxygen depletion dominates at high δ (1.5–2.0), making $\delta \approx 0.7$ the optimal membrane design target. (2) **Enzyme loading optimisation (φ^2 targeting):** operating at $\varphi^2 = 2–4$ maximises sensitivity while avoiding severe oxygen depletion at the electrode surface. (3) **Michaelis constant matching ($\alpha \approx 1$):** selecting GOx variants with $K_{m,glucose} \approx$ expected physiological glucose (5–10 mM) places the enzyme in the maximally responsive region. Wild-type GOx from Aspergillus niger[25] (K_m = 10–33 mM) naturally matches this target. (4) **EIS-guided membrane validation:** implementing the two-step EIS protocol (Section 7.4) to verify $\Delta\theta < 2°$ provides an electrochemical quality control criterion for membrane engineering without requiring a separate oxygen sensor.

8.3. Comparison with Existing Modelling Approaches

The dual-substrate framework distinguishes itself from prior models in three key aspects. First, explicit treatment of oxygen co-substrate limitation through the γ parameter contrasts with single-substrate models that assume oxygen saturation, which fail to predict in vivo behaviour where $\gamma \approx 0.01$ [32]. Second, the semi-analytical RJM/AGM methodology achieves numerical accuracy below 5% error while providing a 250-fold computational speedup (< 1 ms vs. ∼250 ms per evaluation), enabling parametric optimisation studies involving 10 000+ evaluations. Third, the EIS model provides a novel analytical link between dual-substrate kinetics and frequency-domain impedance, yielding the first derivation of the Warburg slope deviation as a quantitative oxygen interference diagnostic — a contribution absent from all prior single-substrate impedance models.

8.4. Model Limitations and Future Extensions

The present model incorporates steady-state and single-layer assumptions. Transient analysis for initial sensor response requires time-dependent reaction-diffusion equations, extendable via Laplace transform methods. Product inhibition by gluconic acid and H_2O_2 at glucose

concentrations above 25 mM, multi-layer membrane geometries, and temperature/pH dependencies of GOx kinetic parameters represent priority extensions. Despite these idealisations, the model captures the dominant physics — dual-substrate oxygen limitation and its electrochemical signatures — responsible for the largest error source in current CGM systems.

9. CONCLUSIONS

This work developed, validated, and electrochemically extended a comprehensive dual-substrate reaction-diffusion framework for glucose oxidase biosensors. The key findings are as follows.

(1) Semi-analytical method agreement. The RJM and AGM produce mutually consistent solutions with mean inter-method relative difference of 3.88%, maximum deviation of 6.93%, and agreement below 7% in 94% of 500 evaluated parameter combinations. Both methods achieve this accuracy at a computational cost below 1 ms per solution, representing a 250-fold speedup relative to refined finite-difference benchmarks.

(2) BRENDA-based model validation. Validation against 17 GOx K_m values from BRENDA (EC 1.1.3.4), grouped into Low (n = 5), Mid (n = 7), and High (n = 5) kinetic categories, yields mean $R^2 = 0.9981$ and fitted $K_{m,app}$ values of 19.1 ± 4.5, 27.4 ± 8.8, and 59.4 ± 52.3 mM. The Low K_m category is recovered with near-perfect fidelity (error 2.3%); systematic underestimation in Mid and High categories (30.3% and 28.5%) reflects sub-saturating calibration data and does not indicate a model deficiency. The mean K_m fitting error of 20.4% lies within the accepted tolerance of ±25–30%.

(3) Kinetic regime delineation. The γ-framework clearly identifies three regimes — oxygen-limited ($\gamma < 0.2$), transition ($0.2 \leq \gamma \leq 1.0$), and glucose-limited ($\gamma > 1.0$) — with critical boundary at $\gamma_{crit} = \beta/\alpha$. Physiological CGM sensors ($\gamma \approx 0.003$–0.01) are confirmed to reside firmly in the oxygen-limited regime, where sensor current reflects tissue oxygen availability rather than glucose concentration.

(4) Diffusivity ratio and membrane design. Increasing $\delta = D_S/D_O$ from 0.1 to 2.0 produces a nearly ten-fold increase in normalised biosensor current. Depletion analysis identifies the transition window δ = 0.5–1.0 as the optimal membrane design target, providing a clear engineering criterion for membrane fabrication.

(5) Sensitivity analysis. Under physiological conditions, oxygen-related parameters (δ, β, γ) collectively account for approximately 70% of first-order output variance. Across the full design space, the normalised glucose K_m (α, $S_t = 0.517$) and Thiele modulus (φ^2, $S_t = 0.425$) emerge as the primary controllers of biosensor response.

(6) Butler–Volmer electrode condition and EIS model. Replacing the passive zero-flux electrode boundary with a Butler–Volmer kinetic condition introduces the parameter Λ and yields an extended semi-analytical solution that recovers the original RJM result exactly as $\Lambda \to 0$. An analytical EIS model, derived from the linearised dual-substrate perturbation equations, predicts Nyquist spectra with a Warburg slope deviation $|\Delta\theta| = 5°–12°$ under physiological CGM conditions ($\gamma = 0.005$) and charge transfer resistance $R_{ct} = 36–90\ \Omega$ for the three BRENDA K_m categories, consistent with published GOx electrode data. The deviation Δθ constitutes a novel single-number experimental diagnostic for oxygen co-limitation: $\Delta\theta > 5°$ identifies the oxygen-limited regime, providing an electrochemically verifiable criterion for membrane engineering quality control without requiring a separate oxygen sensor.

(7) Design implications. Four membrane engineering strategies — optimising δ toward 0.5–1.0, targeting $\varphi^2 = 2–4$ through enzyme loading control, selecting GOx variants with $K_{m,glucose} \approx \alpha \times [S]_{bulk}$, and validating membrane performance via the two-step EIS protocol (Section 7.4) — each derived directly from the quantitative framework, offer a practical pathway toward improved CGM accuracy and reduced need for confirmatory fingerstick measurements.

Funding

This research did not receive any specific grant from funding agencies in the public, commercial, or not-for-profit sectors.

Credit Authorship Contribution Statement

Vaitheeswaran Gnanaraj: Writing – review & editing, Writing – original draft, Visualisation, Software, Project administration, Methodology, Investigation, Formal analysis, Conceptualisation. **Balakrishnan Vellaikannan:** Writing – review & editing, Supervision, Conceptualisation. **Bala Manikandan:** Writing – review & editing, Conceptualisation.

Declaration of Competing Interest

The authors declare that they have no competing financial interests or personal relationships that influenced the work reported in this paper.

Data Availability

The K_m values used in this study were retrieved from the publicly accessible BRENDA Enzyme Database at https://www.brenda-enzymes.org/enzyme.php?ecno=1.1.3.4. No new experimental data were generated. Python solver scripts are available from the corresponding author upon reasonable request.

Acknowledgments

The authors acknowledge Thiagarajar College of Engineering for providing computational facilities.

REFERENCES

[1] Clark, L.C.; Lyons, C. Electrode systems for continuous monitoring in cardiovascular surgery. Ann. N. Y. Acad. Sci. 1962, 102, 29–45. https://doi.org/10.1111/j.1749-6632.1962.tb13623.x

[2] Wang, J. Electrochemical glucose biosensors. Chem. Rev. 2008, 108, 814–825. https://doi.org/10.1021/cr068123a

[3] Gibson, Q.H.; Swoboda, B.E.P.; Massey, V. Kinetics and mechanism of action of glucose oxidase. J. Biol. Chem. 1964, 239, 3927–3934.

[4] Bright, H.J.; Appleby, M. The pH dependence of the individual steps in the glucose oxidase reaction. J. Biol. Chem. 1969, 244, 3625–3634.

[5] Leskovac, V.; Trivić, S.; Wohlfahrt, G.; Kandrac, J.; Pericin, D. Glucose oxidase from Aspergillus niger: the mechanism of action with molecular oxygen, quinones, and one-electron acceptors. Int. J. Biochem. Cell Biol. 2005, 37, 731–750. https://doi.org/10.1016/j.biocel.2004.10.014

[6] Heller, A.; Feldman, B. Electrochemical glucose sensors and their applications in diabetes management. Chem. Rev. 2008, 108, 2482–2505. https://doi.org/10.1021/cr068069y

[7] Wilson, G.S.; Hu, Y. Enzyme-based biosensors for in vivo measurements. Chem. Rev. 2000, 100, 2693–2704. https://doi.org/10.1021/cr990003y

[8] Gerritsen, M.; Jansen, J.A.; Lutterman, J.A. Performance of subcutaneously implanted glucose sensors for continuous monitoring. Neth. J. Med. 1999, 54, 167–179. https://doi.org/10.1016/S0300-2977(99)00004-2

[9] Pickup, J.C.; Hussain, F.; Evans, N.D.; Sachedina, N. In vivo glucose monitoring: the clinical reality and the promise. Biosens. Bioelectron. 2005, 20, 2555–2565. https://doi.org/10.1016/j.bios.2004.10.002

[10] Mell, L.D.; Maloy, J.T. A model for the amperometric enzyme electrode obtained through digital simulation and applied to the immobilized glucose oxidase system. Anal. Chem. 1975, 47, 299–307. https://doi.org/10.1021/ac60352a006

[11] Bartlett, P.N.; Whitaker, R.G. Electrochemical immobilisation of enzymes: Part I. Theory. J. Electroanal. Chem. 1987, 224, 27–35. https://doi.org/10.1016/0022-0728(87)85081-7

[12] Schulmeister, T. Mathematical modelling of the dynamic behaviour of amperometric enzyme electrodes. Sel. Electrode Rev. 1990, 12, 203–260.

[13] Leypoldt, J.K.; Gough, D.A. Model of a two-substrate enzyme electrode for glucose. Anal. Chem. 1984, 56, 2896–2904. https://doi.org/10.1021/ac00278a030

[14] Bartlett, P.N.; Pratt, K.F.E. Modeling of processes in enzyme electrodes. Biosens. Bioelectron. 1993, 8, 451–462. https://doi.org/10.1016/0956-5663(93)80030-S

[15] Martens, N.; Hall, E.A.H. Model for an immobilized oxidase enzyme electrode in the presence of two oxidants. Anal. Chem. 1994, 66, 2763–2770. https://doi.org/10.1021/ac00089a016

[16] Cambiaso, A.; Delfino, L.; Grattarola, M.; Verreschi, G.; Ashworth, D.; Maines, A.; Vadgama, P. Modelling and simulation of a diffusion limited glucose biosensor. Sens. Actuators B Chem. 1996, 33, 203–207. https://doi.org/10.1016/S0925-4005(97)80040-7

[17] Loghambal, S.; Rajendran, L. Mathematical modeling in amperometric oxidase enzyme–membrane electrodes. J. Membr. Sci. 2011, 373, 20–28. https://doi.org/10.1016/j.memsci.2011.02.033

[18] Selvi, S.P.; Nethaji, O.; Vinolyn Sylvia, S.; Rajendran, L. Electrochemical modeling of steady-state diffusion–reaction processes with second-order irreversible kinetics. Int. J. Electrochem. Sci. 2022. https://doi.org/10.20964/2022

[19] Ganji, D.D.; Nourollahi, M.; Mohseni, E. Application of Akbari-Ganji method to nonlinear equations. Dev. Appl. Ocean. Eng. 2014, 3, 22–38.

[20] Salomi, R.J.; Rajendran, L. Cyclic voltammetric response of homogeneous catalysis of electrochemical reactions: Part 1. A theoretical and numerical approach for EE'C scheme. J. Electroanal. Chem. 2022, 918, 116429.

[21] Bartlett, P.N.; Tebbutt, P.; Whitaker, R.G. Kinetic aspects of the use of modified electrodes and mediators in bioelectrochemistry. Prog. React. Kinet. 1991, 16, 55–155.

[22] Gough, D.A.; Lucisano, J.Y.; Tse, P.H.S. Two-dimensional enzyme electrode sensitivity analysis. Anal. Chem. 1985, 57, 2351–2357.

[23] Leskovac, V.; Trivic, S.; Wohlfahrt, G.; Kandrac, J.; Pericin, D. Glucose oxidase from Aspergillus niger. Int. J. Biochem. Cell Biol. 2005, 37, 731–750.

[24] Meena, A.; Rajendran, L. Mathematical modeling of amperometric and potentiometric biosensors and system of non-linear equations — Homotopy perturbation approach. J. Electroanal. Chem. 2010, 644, 50–59.

[25] Priyanka, R. & Muthuramalingam, Rasi & Vani, S. & Rajendran, Lakshmanan & SivaKumar, D.. (2025). A Kinetic Model for Amperometric Biosensor in Dynamic Mode to Various Enzyme Reactions: Theoretical and Numerical Approach. Chemistry Africa. 8. 10.1007/s42250-025-01394-x.

[26] Guan, G.; Qu, L.; Zhao, Y.; et al. Recent advances in glucose monitoring utilizing oxidase electrochemical biosensors integrating carbon-based nanomaterials and smart enzyme design. Front. Chem. 2025, 13, 1591302. https://doi.org/10.3389/fchem.2025.1591302

[27] Lee, I.; Probst, D.; Klonoff, D.; Sode, K. Continuous glucose monitoring systems — Current status and future perspectives of the flagship technologies in biosensor research. Biosens. Bioelectron. 2021, 181, 113054. https://doi.org/10.1016/j.bios.2021.113054

[28] Setford, S.J.; et al. The impact of interfering substances on continuous glucose monitors: Part 1. J. Diabetes Sci. Technol. 2025. DOI: 10.1177/19322968251377027

[29] Cohen, R.; et al. Oxygen insensitive amperometric glucose biosensor based on FAD dependent glucose dehydrogenase co-entrapped with DCPIP or DCNQ in a polydopamine layer. Electrochim. Acta 2021, 367, 137503. DOI: 10.1016/j.electacta.2021.137503

[30] Dixon, B.M.; et al. Characterization in vitro and in vivo of the oxygen dependence of an enzyme/polymer biosensor for monitoring brain glucose. J. Neurosci. Methods 2002, 119, 135–142. DOI: 10.1016/S0165-0270(02)00170-X

[31] Guoqiang, G.; et al. Recent advances in glucose monitoring utilizing oxidase electrochemical biosensors integrating carbon-based nanomaterials and smart enzyme design. Front. Chem. 2025, 13, 1591302. DOI: 10.3389/fchem.2025.1591302

[32] Jayakumar, K.; et al. An oxygen insensitive amperometric glucose biosensor based on an engineered cellobiose dehydrogenase. ChemElectroChem 2022, 9, e202200418. DOI: 10.1002/celc.202200418

[33] Sobol, I.M. Sensitivity analysis for nonlinear mathematical models. Math. Model. Comput. Exp. 1993, 1, 407–414.